Measurement of the negative muon spectrum between 0.3 and 40 GeV/c in the atmosphere

R. Bellotti, F. Cafagna, M. Circella,* G. De Cataldo, C. N. De Marzo,† N. Giglietto, and P. Spinelli
Dipartimento di Fisica dell'Università di Bari and INFN-Sezione di Bari, Via Amendola 173, 70126 Bari, Italy

R. L. Golden, S. A. Stephens,‡ S. J. Stochaj, and W. R. Webber
Particle Astrophysics Laboratory, New Mexico State University, Las Cruces, New Mexico 88003

M. P. De Pascale, A. Morselli, and P. Picozza
Dipartimento di Fisica dell'Università di Roma "Tor Vergata" and INFN-Sezione di Roma II, Via Carnevale 15, 00173 Rome, Italy

J. F. Ormes and R. E. Streitmatter
NASA Goddard Space Flight Center, Greenbelt, Maryland 20771

F. Massimo Brancaccio, P. Papini, P. Piccardi, and P. Spillantini
Dipartimento di Fisica dell'Università di Firenze and INFN-Sezione di Firenze, Largo Enrico Fermi 2, 50125 Florence, Italy

G. Basini, F. Bongiorno,§ and M. Ricci
INFN Laboratori Nazionali di Frascati, Via Enrico Fermi 40, 00044 Frascati, Italy

M. T. Brunetti, A. Codino, C. Grimani, M. Menichelli, and I. Salvatori
Dipartimento di Fisica dell'Università di Perugia and INFN-Sezione di Perugia, Via Giovanni Pascoli, 06100 Perugia, Italy

(Received 12 July 1995)

A measurement of the negative muon flux in the atmosphere has been made using a superconducting magnet spectrometer during the ascent part of a balloon flight experiment performed on September 5, 1989 from Prince Albert, Saskatchewan (Canada). The negative muon component has been measured over the momentum range 0.3–40 GeV/c with an altitude increasing from 0.6 to 36 km above sea level. This is the first time that results from such wide intervals in momentum and atmospheric depth have been obtained using a single apparatus. The flux growth curve with atmospheric depth is momentum dependent; the low energy muon flux peaks around 150 g/cm^2 and higher energy muons penetrate to larger depths in the atmosphere. The flux decreases exponentially with increasing depth above 200 g/cm^2. The attenuation length Λ_e increases almost linearly with the muon momentum at a rate of about 90 (g/cm^2)/(GeV/c) in the 0.3–8 GeV/c range. The momentum spectra at different altitudes can be described by power-laws, provided that the spectral index is left free to change with altitude. We found that an index value of -2.5 ± 0.2 can give a good description of the data for momenta between 2 and 40 GeV/c in the depth range 20–400 g/cm^2. Below 1 GeV/c, the spectrum gradually steepens as the atmospheric depth decreases. Above 600 g/cm^2 a peak around 0.5 GeV/c arises.

PACS number(s): 96.40.Tv, 14.60.Pq

I. INTRODUCTION

The main source of muons in the atmosphere in the momentum range below 40 GeV/c is the decay of pions produced in hadronic interactions of cosmic rays (e.g., [1]). The contribution from kaon decay is only important above a few hundred GeV/c. Recently, the opportunity to use this information as a check on cosmic ray cascade calculations and for calibration of atmospheric neutrino calculations has created a renewed interest in the muon spectra as a function of the atmospheric depth (e.g., [2,3]). Preliminary values of the measurements presented in this paper have been already used as input data to calculations of the atmospheric neutrino flux with the hope to shed light on the problem of the atmospheric

*Electronic address: circella@axpba0.ba.infn.it
†Electronic address: demarzo@axpba0.ba.infn.it
‡Also at Tata Institute of Fundamental Reseaarch, Bombay, India.
§Now at Dipartimento di Elettronica della III Università di Roma, Rome, Italy.

neutrino anomaly [4].

Detailed calculations of the muon flux in the atmosphere are very difficult to perform, especially at low energy where one needs to take into account the details of particle propagation and interactions. Analytic approaches have been succesfully undertaken in the past since the pioneering work by Stephens ([5]; see also [3]), even though Monte Carlo techniques are usually preferred.

While sea-level measurements are widely reported in the literature, there are very few measurements of the muon flux as a function of altitude [6,7]. The latter experiments were carried out either with airplane-borne apparatus or at mountain sites. Counter telescopes were used for detecting charged particles and muons were selected by requiring them to traverse large amounts of matter without interacting. The main difficulty in performing a muon measurement at or above stratospheric altitudes is to properly compensate for the contamination of the muon sample by other particles. This problem becomes even more complex for positive muon measurements, since the proton flux strongly increases with altitude.

This paper reports a study of the atmospheric muon flux at various altitudes from 0.6 to 36 km carried out by analyzing the events recorded by the Matter Antimatter Spectrometer System (MASS) apparatus during its ascent in a balloon flight. Although the main objective of the mission was to measure the antiproton flux at the top of the atmosphere, the apparatus was able to recognize negative muons with good efficiency and low background, as shown in the next sections. The sample of 2893 negative muons obtained at various altitudes provides the most extensive observation in the literature. The experiment was performed on September 5, 1989 starting from Prince Albert, Saskatchewan (Canada) at 600 m above sea level. The coordinates of this location are 53°N and 106°W, corresponding to a cutoff rigidity of about 0.65 GV. The apparatus reached a float altitude of about 36 km after an ascent that lasted almost 3 h. The data sample included more than 360 000 events, gathered over a period of 9855 s. Results on the negative muon spectrum in the momentum interval 0.3–40 GeV/c are presented in this paper. Preliminary results of this analysis were reported earlier [8]. A measurement of the muon flux and charge ratio at the ground level has already been published [9].

II. MASS APPARATUS

The MASS apparatus, shown in Fig. 1, consisted of (1) a superconducting magnetic rigidity spectrometer using eight multiwire proportional chambers (MWPC's), (2) a time of flight (TOF) system with two planes having two layers each of scintillators to indicate the direction of travel, (3) a high resolution scintillator for ionization loss rate measurement, and (4) a gas Cherenkov detector and (5) a streamer tube imaging calorimeter to aid in particle identification. A coincidence between the TOF scintillators gave the trigger for data acquisition.

The superconducting magnet was operated at a current of 120 A, producing a magnetic field of 10–40 kG in the MWPC region. The maximum detectable rigidity for this configuration of the spectrometer was more than 100 GV [10]. The MWPC signals were fed to delay lines and the times of arrival at each end of the delay lines were measured [11]. The sum of the delay line readout times was required to be equal to the total delay of the line, in order to accept an event. All of the chambers were equipped with a readout along the x axis (where most of the curvature occurred) and four of them were also read in the y view.

The Cherenkov detector was filled with a 50-50 mixture of Freon 12 and Freon 22 with a threshold Lorentz factor $\gamma_{th} \approx 23$. Signals from the TOF scintillators, the high resolution scintillator, and the Cherenkov detector were pulse height analyzed.

The calorimeter consisted of 40 layers of 64 brass streamer tubes each. Tubes from adjacent layers were arranged perpendicular to each other. The total depth of the calorimeter was 40 cm, equivalent to 7.3 radiation lengths and 0.7 interaction lengths for protons. More details on the apparatus characteristics and performances are given elsewhere [12,10,9].

III. DATA ANALYSIS

A. Event selection

All of the criteria used for event selection are reported in Table I. Both reliability tests on the track reconstruc-

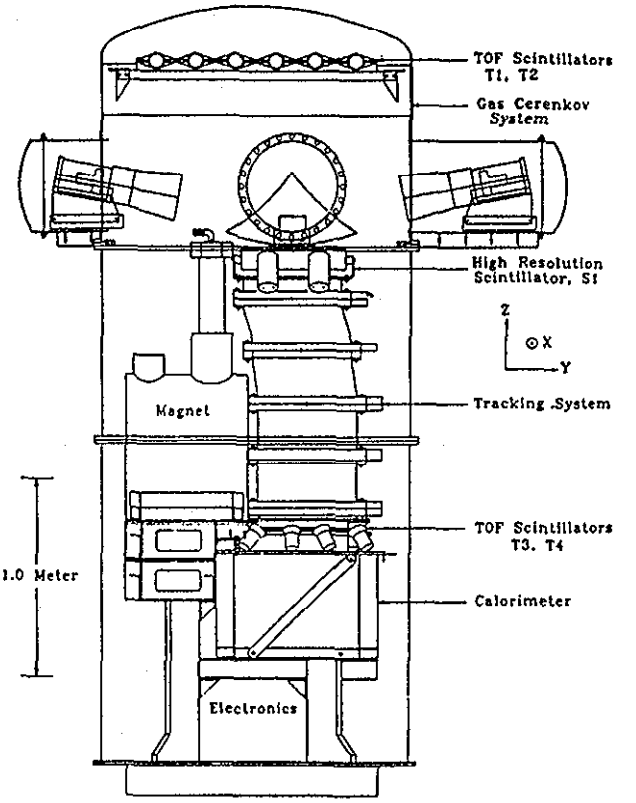

FIG. 1. The MASS apparatus.

TABLE I. Selection criteria.

Test	Description
1	A minimum of five out of 8 x-view and three out of four y-view MWPC's, with proper location in the spectrometer, giving good time sum measurements
2	$\chi_x^2 \leq 5$ and $\chi_y^2 \leq 7.5$ for the reconstructed track
3	A deflection uncertainty $\sigma_\eta \leq 0.03$ GV^{-1}
4	Signals S from $T1$ and $T3$ such that $0.5I_0 \leq S \leq 2I_0$
5	A number of hits, N, in the calorimeter such that $2 \leq N \leq 9$ in the x- and y-view upper part and $3 \leq N \leq 12$ in the x-view lower part

tion and muon identification criteria were considered. For the former purpose, tests 1–3 in Table I were found to be essential (see [10], for an extensive discussion). Tests 4 and 5 were introduced for selection of the muon signal against background with cuts on the pulse height distribution in the scintillators and the hit tube pattern in the calorimeter: Muons were required to appear as minimum ionizing singly charged particles in two layers of scintillators (hereinafter referred to as $T1$ and $T3$, respectively) and not to show an interaction in the calorimeter. The latter condition was imposed by considering the calorimeter divided into two nearly equal upper and lower parts and by selecting events with a proper number of hits in each part—the lower y-view part was not operated during the flight. The symbol I_0 in test 4 stands for the mean pulse height in the scintillator for a minimum ionizing singly charged particle.

The velocity measurement from the time of flight as well as the Cherenkov pulse height was also considered in the analysis, as explained in the next subsection.

A total number of 3235 negative curvature events were found to pass the tests in Table I and were selected for further analysis.

B. Background estimates and corrections

Special care was devoted in estimating the degree of possible contamination of the measurements by particles other than muons. Possible background sources are listed in Table II, along with the procedures adopted to correct for them. The estimated residual contamination that can affect the final results of the analysis is also shown. One may note that the contamination is expected to have a dependence on both altitude and energy. This dependence was carefully studied in order to make the necessary corrections.

Albedo events are upward-going positive particles simulating a negative curvature in the magnetic field. Most of these events arise from low energy protons impinging at large zenith angles which are scattered upward in interactions below the apparatus. The 432 upward-going particles found in the whole sample of negative curvature events were mostly concentrated toward the low atmospheric depths and around rigidities of 0.4 GV. The criteria used for muon selection and the scintillator test in particular were found to be very effective in order to remove these events. The few upward-going particles that survived the prior selection were finally rejected by means of a direct test of the β measurement from the time of flight, as shown in Table II.

The electron flux in the atmosphere consists of a primary and a secondary component, the relative contributions to the total flux depending on the altitude and the energy of the particles. For energies $\lesssim$1 GeV, a broad peak is reached at atmospheric depths of 100–150 g/cm^2 and the flux will rapidly decrease with increasing depth after this maximum ([13], and references therein). The muon flux is expected to reach its maximum value deeper in the atmosphere. Also, the momentum spectrum is expected to be less steep for muons than for electrons at low momentum [14,1]. For these reasons, it may be expected that the worst conditions for the relative ratio of muon to electron flux will occur at the lowest momentum and at less than 100 g/cm^2.

The degree of possible contamination of the muon sample by electrons can be realized from Fig. 2, in which the fraction of muonlike events which are accompanied with a Cherenkov signal is shown. The events in Fig. 2 were selected with the muon selection criteria (tests 1–5 in Table I) and were also required to pass the β requirement in Table II. The threshold rigidity for muons to give a Cherenkov signal occurs at 2.4 GV. Muonlike events with a Cherenkov signal far below this threshold were interpreted as contaminating electrons and removed from the sample. They are mostly distributed at very low rigidities and their number goes rapidly to zero above 1 GV. The fraction of events which were accompanied with a

TABLE II. Background sources.

Source	Correction	Residual contamination
Albedo	$\beta \geq 0.8$	none
Electrons	Cherenkov pulse height less than the equivalent to one photoelectron at rigidities $R \lesssim 1.5$ GV	$\lesssim$1% at less than 1 GeV/c negligible at higher momenta
Spillover protons	spillover subtraction at rigidities $R \geq 8$ GV	negligible
Mesons	no correction	$\lesssim$1% almost everywhere for pions negligible for kaons

Cherenkov signal reached a value of 97% in the rigidity interval 4–8 GV, which increased to more than 98% if only the events passing through the central part of the detector were selected for this purpose. The latter result is quite consistent with the value of detector efficiency which was determined previously [12]. From an assumed inefficiency of 3% for detecting particles far above the threshold and the ratio in Fig. 2, the residual low energy electron contamination in Table II can be estimated.

The fraction of events with a Cherenkov signal from Fig. 2 shows a value of 90% at rigidities greater than 8 GV. Spillover may be responsible for this smaller value. If a Cherenkov efficiency of 97% is assumed, a total of 13 contaminating events can be estimated in the 8–100 GV interval, which is not inconsistent with the 16 spillover events expected in this region.

Spillover events are particles whose sign is misinterpreted in the magnet spectrometer. This situation can occur more easily at high rigidity, where the track curvature becomes comparable to the measurement resolution of the MWPC's. The number of expected spillover events was estimated by convolution of the spectrum of positive particles surviving the negative muon selection with the resolution function of the spectrometer. It was found that spillover may become a major source of background at rigidities greater than 8 GV, especially at small atmospheric depths where the proton flux is larger. The number of expected spillover events was subtracted from the high energy muon sample. No correction was necessary at lower momenta.

Finally, in the meson (namely, pion and kaon) case, the relative ratio of fluxes can also be expected to be a function of altitude and energy. After a comparison of the present results to theoretical calculations of meson fluxes at several altitudes and energies in the atmosphere [1], it was estimated that an altitude-dependent pion contamination of the order of (1–2)% could be present in the muon sample in the depth interval 25–250 g/cm^2. The kaon contamination will be much smaller and therefore absolutely negligible for this analysis.

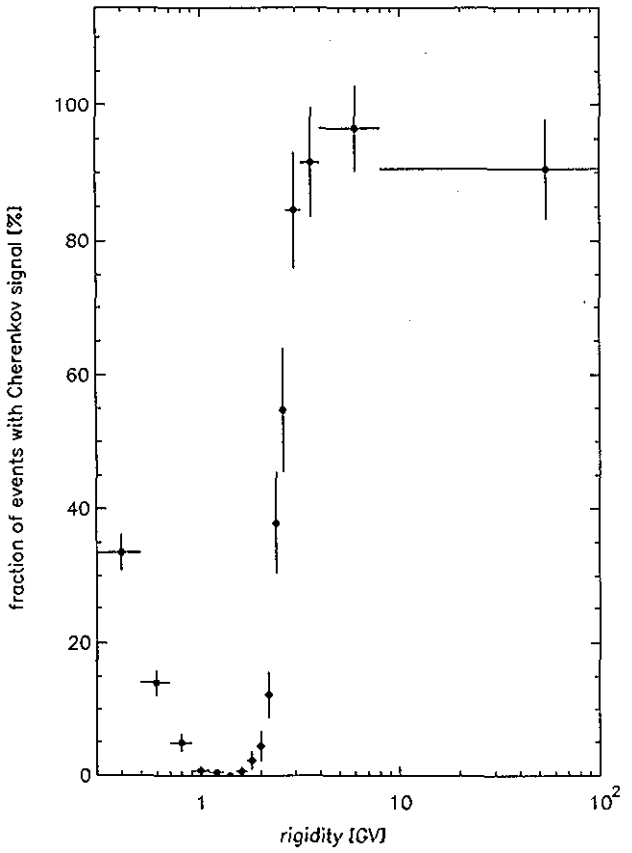

FIG. 2. Fraction of negative muonlike events accompanied with a Cherenkov signal as a function of magnetic rigidity.

C. Geometric factor and efficiencies

The geometric factor of the apparatus was calculated for particles that entered from the uppermost layer of the TOF scintillators and left through the bottom layer of the calorimeter. It is a function of particle rigidity and it ranges from 77.6 cm^2 sr at 0.3 GV to 127.8 cm^2 sr at $R \geq 5$ GV for negative particles. There exists a small difference between positive and negative particles due to a mechanical asymmetry of the magnet with respect to the detector stack. The geometric factor calculations are accurate to the order of 0.1%. The MWPC efficiency also shows a dependence on deflection, as discussed in Ref. [9]. It increases from 0.51±0.03 at about 0.3 GV to a plateau value of 0.69±0.01 above 2 GV for negative particles.

Signals from one layer of the upper set of scintillators and one of the lower set were considered for event selection. Such a combination can help improve the rejection of nonminimum ionizing particles because of the small amount of energy (≈10 MeV at minimum ionization) that a particle will lose while traversing the apparatus and it can have a larger effect on the selection of low energy positive muons. The scintillator efficiency was studied with the aid of the signal from the high resolution scintillator $S1$. The float altitude high energy proton sample was considered for this purpose and their pulse heights from $S1$, $T1$, and $T3$ carefully studied. Finally, an efficiency of 89% was estimated for the scintillator selection, which is quite consistent with previous studies [9].

The calorimeter efficiency for detection of noninteracting particles which satisfy test 5 in Table I was studied by carefully examining the topology of each event which failed to pass the requirement. The streamer tube inefficiency as well as the noise can lead to a failure of the test. A global selection efficiency of 80% was estimated, in good agreement with that found in the ground analyses [9]. Also, a large sample of particles passing test 5 was scanned, in order to check for interacting particle contamination. No evidence of electromagnetic showers or interactions in the calorimeter was found in the muon sample at rigidities larger than 1.5 GV. The time dependence of both the calorimeter and scintillators responses was accurately studied and no significant variation with

TABLE III. Apparatus efficiency.

Detector or function	Efficiency
MWPC	Energy dependent below 2 GeV/c
	0.69±0.01 above 2 GeV/c
Scintillators	0.89±0.01
Calorimeter	0.80±0.01
TOF	0.98
Tape reading	0.97
Trigger	0.82±0.01
Live-time fraction	Time dependent
	Between 0.65 and 0.68 at less than 130 g/cm^2

time was observed.

The velocity selection, as in Table II, introduced a 98% efficiency, because some configurations of the scintillator paddles were not suitable for a TOF measurement and as a consequence a fraction of the events had to be removed from the analysis. Efficiencies were also introduced in order to compensate for the tape transferring process (97%) and trigger efficiency (82%) [9]. On the contrary, no correction was necessary for the Cherenkov test at low energy since the probability for a particle below threshold to be accompanied with a noise pulse larger than the equivalent to one photoelectron had been estimated to be negligible [12].

In evaluating the absolute fluxes, the exposure time as well as the dead time fraction was considered. The latter was time dependent since the trigger rate changed considerably during the ascent. The recording efficiency due to the dead time (hereafter referred to as "live-time fraction") varied between 0.98 at altitudes close to ground and 0.68 at float altitude. It changed slowly at altitudes greater than 15 km (atmospheric depths less than 130 g/cm^2).

All of the efficiencies considered in this analysis are reported in Table III, along with the estimated errors, if not negligible. The global efficiency for detection of negative muons ranged from 0.184±0.011 at 300 MeV/c at maximum dead time to 0.375±0.009 above 2 GeV/c at minimum dead time. For the global systematic uncertainty on the detection efficiency we can set an upper limit at 5%, based on our knowledge of the apparatus used in these as well as in other measurements. Both statistical fluctuations of the number of events and the estimated uncertainties of the detection efficiencies are included in the results. Gaussian errors were assumed for muon event fluctuations and also for background events.

IV. RESULTS

A sample of 2893 negative muons was finally selected with all of the criteria from Table I and Table II, in the momentum range 0.3–40 GeV/c. Since they were recorded during the ascent of the flight, they were distributed between 910 and 5 g/cm^2 in atmospheric depth. Figure 3 shows the ascent curve of the apparatus, as measured during the NSBF (National Scientific Balloon Facility) control operation. The accuracy with which the atmospheric depth can be determined at each time is of the order of 1%.

A. Flux growth curve

The altitude dependence of the negative muon flux was separately investigated in different momentum intervals. Independent growth curves in the atmosphere were built in the different momentum bins, with the constraints im-

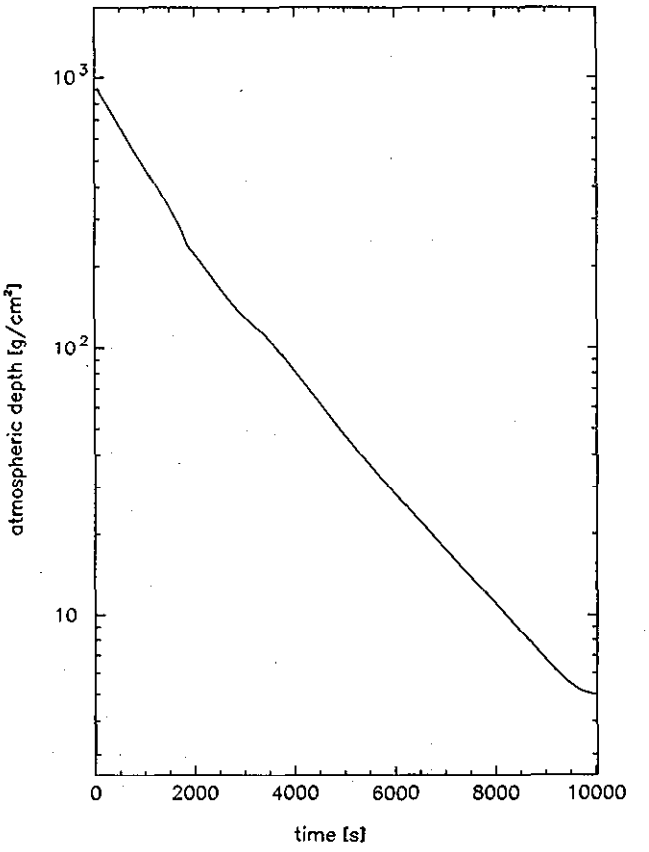

FIG. 3. Ascent curve of the apparatus.

TABLE IV. Flux growth curve results for negative muons in the 0.3–40 GeV/c momentum range. Results are given for the following momentum intervals (average values are shown in Fig. 4): (I) 0.3–0.53 GeV/c, (II) 0.53–0.75 GeV/c, (III) 0.75–0.97 GeV/c, (IV) 0.97–1.23 GeV/c, (V) 1.23–1.55 GeV/c, (VI) 1.55–2 GeV/c, (VII) 2-3.2 GeV/c, (VIII) 3.2–8 GeV/c, (IX) 8–40 GeV/c.

Depth interval		*A*	*B*	*C*	*D*
Duration (s)		635	630	520	470
Live-time fraction		0.98	0.91	0.84	0.77
Initial depth (g/cm^2)		910	587	381	243
Final depth (g/cm^2)		587	381	243	190
APD[a] (g/cm^2)		736	477	313	215
I	Flux[b]	$1.93\pm0.70\times10^{-3}$	$4.9\pm1.1\times10^{-3}$	$1.12\pm0.20\times10^{-2}$	$1.46\pm0.26\times10^{-2}$
	FAD[c] (g/cm^2)	702.6	466.0	309.6	215.1
II	Flux[b]	$2.12\pm0.62\times10^{-3}$	$5.6\pm1.1\times10^{-3}$	$1.05\pm0.17\times10^{-2}$	$1.24\pm0.20\times10^{-2}$
	FAD[c] (g/cm^2)	706.5	467.8	310.3	215.2
III	Flux[b]	$2.10\pm0.59\times10^{-3}$	$5.6\pm1.0\times10^{-3}$	$8.3\pm1.4\times10^{-3}$	$1.00\pm0.17\times10^{-2}$
	FAD[c] (g/cm^2)	707.4	468.1	310.5	215.3
IV	Flux[b]	$2.08\pm0.52\times10^{-3}$	$4.50\pm0.81\times10^{-3}$	$6.1\pm1.1\times10^{-3}$	$8.4\pm1.4\times10^{-3}$
	FAD[c] (g/cm^2)	708.9	468.8	310.8	215.3
V	Flux[b]	$1.56\pm0.40\times10^{-3}$	$3.93\pm0.67\times10^{-3}$	$4.74\pm0.85\times10^{-3}$	$6.2\pm1.1\times10^{-3}$
	FAD[c] (g/cm^2)	710.0	469.3	311.0	215.3
VI	Flux[b]	$1.33\pm0.31\times10^{-3}$	$2.39\pm0.44\times10^{-3}$	$3.79\pm0.64\times10^{-3}$	$4.29\pm0.74\times10^{-3}$
	FAD[c] (g/cm^2)	711.8	470.0	311.4	215.4
VII	Flux[b]	$9.4\pm1.6\times10^{-4}$	$1.52\pm0.22\times10^{-3}$	$1.81\pm0.27\times10^{-3}$	$1.98\pm0.31\times10^{-3}$
	FAD[c] (g/cm^2)	714.6	471.2	311.9	215.5
VIII	Flux[b]	$3.17\pm0.47\times10^{-4}$	$4.32\pm0.58\times10^{-4}$	$4.03\pm0.64\times10^{-4}$	$4.36\pm0.72\times10^{-4}$
	FAD[c] (g/cm^2)	719.7	473.4	312.9	215.6
IX	Flux[b]	$2.37\pm0.50\times10^{-5}$	$2.00\pm0.48\times10^{-5}$	$1.76\pm0.51\times10^{-5}$	$1.74\pm0.56\times10^{-5}$
	FAD[c] (g/cm^2)	723.9	475.1	313.6	215.7

Depth interval		*E*	*F*	*G*	*H*
Duration (s)		430	490	560	600
Live-time fraction		0.72	0.69	0.68	0.67
Initial depth (g/cm^2)		190	149	120	92
Final depth (g/cm^2)		149	120	92	66
APD[a] (g/cm^2)		169	133	107	78
I	Flux[b]	$1.84\pm0.31\times10^{-2}$	$1.55\pm0.28\times10^{-2}$	$1.51\pm0.26\times10^{-2}$	$1.37\pm0.23\times10^{-2}$
	FAD[c] (g/cm^2)	168.8	133.4	107.1	79.0
II	Flux[b]	$1.09\pm0.20\times10^{-2}$	$1.11\pm0.20\times10^{-2}$	$9.4\pm1.7\times10^{-3}$	$8.3\pm1.6\times10^{-3}$
	FAD[c] (g/cm^2)	168.8	133.5	107.1	79.0
III	Flux[b]	$1.00\pm0.18\times10^{-2}$	$1.05\pm0.18\times10^{-2}$	$8.7\pm1.6\times10^{-3}$	$7.1\pm1.4\times10^{-3}$
	FAD[c] (g/cm^2)	168.8	133.5	107.1	79.0
IV	Flux[b]	$8.0\pm1.5\times10^{-3}$	$7.4\pm1.4\times10^{-3}$	$6.2\pm1.2\times10^{-3}$	$5.8\pm1.1\times10^{-3}$
	FAD[c] (g/cm^2)	168.9	133.5	107.1	79.0
V	Flux[b]	$5.6\pm1.1\times10^{-3}$	$4.97\pm0.98\times10^{-3}$	$3.90\pm0.82\times10^{-3}$	$3.70\pm0.78\times10^{-3}$
	FAD[c] (g/cm^2)	168.9	133.5	107.1	79.0
VI	Flux[b]	$3.98\pm0.77\times10^{-3}$	$3.80\pm0.72\times10^{-3}$	$3.01\pm0.61\times10^{-3}$	$2.86\pm0.58\times10^{-3}$
	FAD[c] (g/cm^2)	168.9	133.5	107.1	79.0
VII	Flux[b]	$2.15\pm0.35\times10^{-3}$	$2.14\pm0.33\times10^{-3}$	$1.76\pm0.28\times10^{-3}$	$1.33\pm0.24\times10^{-3}$
	FAD[c] (g/cm^2)	169.0	133.6	107.2	79.1
VIII	Flux[b]	$4.55\pm0.80\times10^{-4}$	$3.81\pm0.70\times10^{-4}$	$3.38\pm0.62\times10^{-4}$	$3.42\pm0.61\times10^{-4}$
	FAD[c] (g/cm^2)	169.0	133.6	107.2	79.1
IX	Flux[b]	$1.80\pm0.63\times10^{-5}$	$2.63\pm0.72\times10^{-5}$	$1.45\pm0.52\times10^{-5}$	$1.85\pm0.57\times10^{-5}$
	FAD[c] (g/cm^2)	169.1	133.6	107.2	79.1

TABLE IV. (*Continued*).

Depth interval		*I*	*J*	*K*
Duration (s)		1180	1760	2580
Live-time fraction		0.66	0.67	0.68
Initial depth (g/cm^2)		66	36	15
Final depth (g/cm^2)		36	15	5
APD[a] (g/cm^2)		49	24	9
I	Flux[b]	$1.00\pm0.14\times10^{-2}$	$5.8\pm1.2\times10^{-3}$	$2.04\pm0.59\times10^{-3}$
	FAD[c] (g/cm^2)	50.3	24.9	9.7
II	Flux[b]	$6.34\pm0.99\times10^{-3}$	$4.07\pm0.70\times10^{-3}$	$1.26\pm0.37\times10^{-3}$
	FAD[c] (g/cm^2)	50.4	24.9	9.7
III	Flux[b]	$4.26\pm0.76\times10^{-3}$	$2.84\pm0.52\times10^{-3}$	$9.8\pm2.6\times10^{-4}$
	FAD[c] (g/cm^2)	50.4	24.9	9.8
IV	Flux[b]	$3.63\pm0.62\times10^{-3}$	$1.72\pm0.35\times10^{-3}$	$7.4\pm1.9\times10^{-4}$
	FAD[c] (g/cm^2)	50.4	24.9	9.8
V	Flux[b]	$2.98\pm0.50\times10^{-3}$	$1.48\pm0.29\times10^{-3}$	$6.3\pm1.5\times10^{-4}$
	FAD[c] (g/cm^2)	50.4	24.9	9.8
VI	Flux[b]	$2.23\pm0.37\times10^{-3}$	$1.02\pm0.20\times10^{-3}$	$3.41\pm0.95\times10^{-4}$
	FAD[c] (g/cm^2)	50.4	24.9	9.8
VII	Flux[b]	$8.6\pm1.4\times10^{-4}$	$3.22\pm0.69\times10^{-4}$	$1.87\pm0.43\times10^{-4}$
	FAD[c] (g/cm^2)	50.4	24.9	9.9
VIII	Flux[b]	$1.65\pm0.30\times10^{-4}$	$7.3\pm1.6\times10^{-5}$	$4.9\pm1.1\times10^{-5}$
	FAD[c] (g/cm^2)	50.5	24.9	9.9
IX	Flux[b]	$1.17\pm0.33\times10^{-5}$	$5.1\pm1.9\times10^{-6}$	$3.7\pm1.4\times10^{-6}$
	FAD[c] (g/cm^2)	50.5	24.9	9.9

[a]APD stands for average payload depth.
[b]Units of flux are particles/(cm^2 s sr GeV/c).
[c]FAD stands for flux-weighted average payload depth.

posed by the flux values at ground level and float altitude, as measured with the same apparatus [9,15]. It was found that a curve of the form

$$\Phi(X) = kXe^{-X/\Lambda}, \tag{4.1}$$

Φ being the muon flux in a momentum bin, X being the atmospheric depth, and k and Λ being free to change in order to best fit the data, can give a good interpolation of the measurements, except at very low momenta where the flux undergoes a sudden attenuation soon after reaching a maximum around 150 g/cm^2.

The flux growth curves for nine momentum intervals are reported in Table IV. A growth curve as in (4.1) with the best-fit values of the parameters k and Λ was used for estimating the flux-weighted average values of atmospheric depth (FAD) shown along with the measured fluxes in Table IV. These results are plotted in Fig. 4. Average values of atmospheric depth during the payload ascent (APD) are also shown in Table IV.

Investigations of the altitude dependence of the flux require small momentum intervals in order to have minimum spectral variations with changing altitudes. On the other hand, larger bin widths are preferred in order to minimize the statistical fluctuations, especially when dealing with small samples of events. The momentum intervals used in Table IV are the best compromise between these two constraints. As a consequence, average values of momentum can be calculated in each momentum interval and the spectral variations with altitude will not affect these estimates more than the estimated statistical uncertainties [(1–2)%, typically]. They are shown in Fig. 4.

As a close investigation of Fig. 4 reveals, the flux growth curves do not scale with the muon momentum. In particular, we note that the broad peak in the curves moves from around 150 g/cm^2 toward 200 g/cm^2 with increasing momentum from below 0.5 GeV/c up to a few GeV/c. At the same time, the flatness of the growth curves at larger depths increases with increasing momenta. If a parametrization as in (4.1) is adopted, the best-fit value of Λ increases from $\Lambda = 192 \pm 3$ g/cm^2 to $\Lambda = 216 \pm 3$ g/cm^2 and $\Lambda = 268 \pm 4$ g/cm^2, respectively in the intervals 0.3–0.75 GeV/c, 0.75–1.55 GeV/c, and 1.55–8 GeV/c. In this case, the average muon energy changes from below to above the energy ε_μ, at which the mean path of a muon before decaying equals the atmospheric scale height, being $\varepsilon_\mu \approx 1$ GeV at stratospheric depths [16]. The momentum dependence of the flux growth curve will correspond to an altitude dependence of the muon momentum spectra, as commented on in the next subsection.

Difficulties arise when trying to interpolate the measurements at low energy and high depth with a curve

as in (4.1). Unfortunately, no detailed calculations are available in the literature in these ranges of energy and altitude for a cross-check of the theory as well as of the measurements. In a simplified model of the muon propagation in the atmosphere, taking into account the energy losses and the energy-dependent muon decay probability, we calculated the muon spectrum on the ground from the lowest altitude measurements and vice versa. We did not find any evidence of contradiction between the two sets of data.

It may be pointed out that an exponential attenuation can give a better interpolation of the measurements deep in the atmosphere than the growth curve in (4.1). Our best-fit values for the exponential attenuation length Λ_e in the 190–910 g/cm^2 range are $\Lambda_e = 345 \pm 17$ g/cm^2, $\Lambda_e = 378 \pm 14$ g/cm^2, and $\Lambda_e = 571 \pm 30$ g/cm^2, in the intervals 0.3–0.75 GeV/c, 0.75–1.55 GeV/c, and 1.55–8 GeV/c, respectively. We also found an almost linear dependence of Λ_e with the average momentum of muons in the 0.3–8 GeV/c range, with an increasing rate of about 90 (g/cm^2)/(GeV/c).

Conversi [6] investigated the altitude dependence of the muon and proton flux in the depth range 231–1010 g/cm^2. Muons were identified by means of a delayed coincidence technique. They were stopped in a 10 cm graphite absorber, after traversing 6 in. of lead and the resulting momentum interval was 315–348 MeV/c. Corrections were introduced in order to refer all the measurements to the same latitude of 50°N. An exponential fit with an attenuation length $\Lambda_e = 280$ g/cm^2 was found to give a good interpolation of the total muon data. This value is not inconsistent with $\Lambda_e = 347 \pm 41$ g/cm^2 that we found for the ascent negative muon flux between 300 and 530 MeV/c in the depth range 190–910 g/cm^2. It should be noted that the flux dependence on altitude may be different for muons of different charges, reflecting the different interaction properties of protons and neutrons. Also, our average momentum is higher than in Ref. [6].

Blokh *et al.* [7] reported measurements of the muon flux between 600 and 1000 mbar taken on Mount Elbrus. They used a 10 cm lead shield with a resulting momentum threshold lower than 300 MeV/c. Only integral flux measurements of muons of either charges above this momentum threshold are available in this case, and therefore a comparison with either the present results or those by Conversi [6] is difficult.

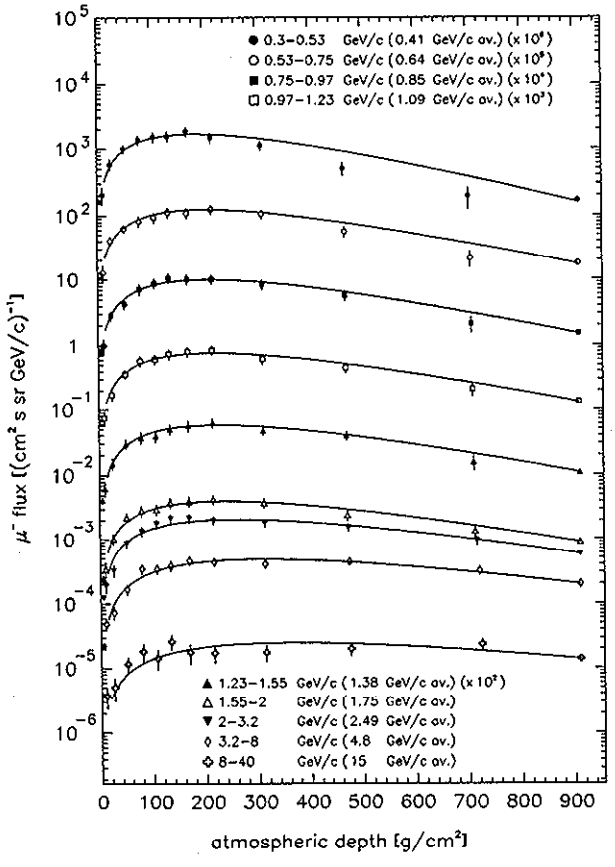

FIG. 4. Flux growth curves for negative muons in the 0.3–40 GeV/c momentum range. Results are plotted for various momentum intervals. The corresponding average values of momentum are shown. Some of the distributions have been scaled as indicated. The measurements at the highest and lowest depths are from Refs. [9] and [15], respectively. Best-fit curves of the form (4.1) are superimposed.

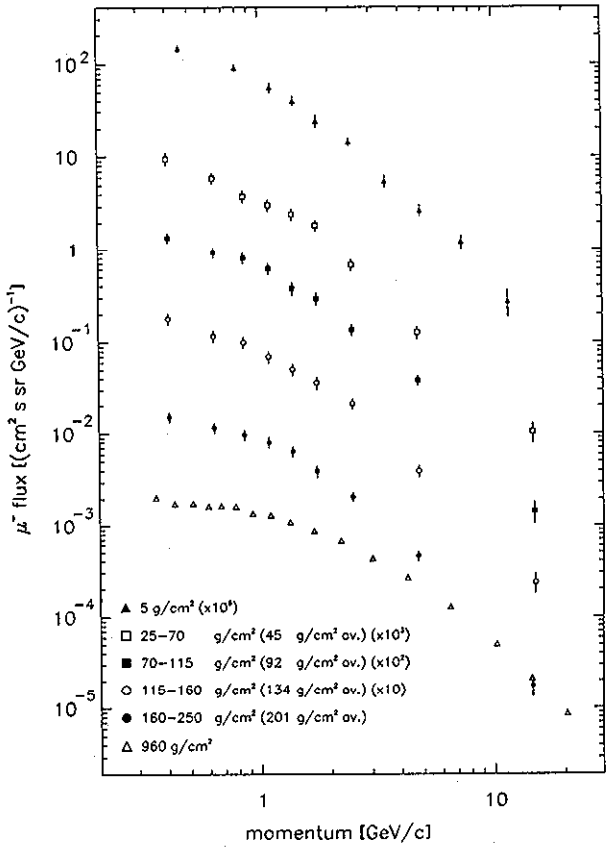

FIG. 5. Negative muon momentum spectra at various depths in the atmosphere. The depth ranges are shown, and the corresponding average values as well. Some of the distributions have been scaled as indicated. Measurements at the ground level (960 g/cm^2) and at 5 g/cm^2 atmospheric depth are also shown (Refs. [9] and [15], respectively).

B. Momentum spectrum

The negative muon momentum spectra at four different average atmospheric depths are shown in Fig. 5. The data for this figure correspond to the depth interval between 250 and 25 g/cm^2, where the momentum dependence of the flux growth curve is so smooth that the differences among the mean atmospheric depths in different momentum intervals are much less than 1%, as can be seen in Table IV. In some cases, the flux-weighted average values of depth also differ negligibly from the corresponding average working depths of the apparatus and this is an indication that a linear dependence of the flux on the atmospheric depth can give a good approximation within the pressure interval considered. An accuracy of 1% has to be assumed on the values of average atmospheric depth shown in Fig. 5. The flux is plotted at mean momentum values from a flux-averaged estimate. A power-law distribution was assumed for this purpose:

$$\Phi(P) \propto P^{\alpha}, \tag{4.2}$$

with the power index α left free to change with momentum and depth in order to best fit the data. We found that, while, below 1 GeV/c, α gradually decreases from a small positive value above 600 g/cm^2 to ≈ -1 at the lowest atmospheric depth, it stays almost constant above 2 GeV/c, $\alpha = -2.5 \pm 0.2$, giving a good description of the spectrum between 20 and 400 g/cm^2.

V. CONCLUSIONS

A study of the muon component in the atmosphere has been carried out by means of a single apparatus during the ascent of a balloon flight at high latitude. The depth range covered in this experiment is between 5 and 910 g/cm^2. The momentum interval investigated ranges from 0.3 to 40 GeV/c. The altitude dependence of the negative muon flux has been studied in nine momentum intervals. It has been shown that the flux growth curve in the atmosphere does not scale with the muon momentum. Also, the negative muon momentum spectra have been measured in four depth ranges. Spectral variations, as well as intensity variations, have been found with changing altitude. However, an altitude-independent power-law representation of the data is possible at momenta between 2 and 40 GeV/c in a wide range of atmospheric depth.

To judge the consistency of the present measurements with the rather scanty previous data is not a straightforward matter, even though no contradiction seems to appear.

The measured spectra can provide constraints to, and improve the precision of calculations of, the atmospheric neutrino fluxes. Further information will be derived by an analysis of the positive muon data from the same flight. A new dedicated flight aimed at an extensive exploration of the secondary particles in the atmosphere with better statistical precision is being planned.

ACKNOWLEDGMENTS

We would like to thank the National Scientific Balloon Facility (Palestine, Texas) for providing us with their measurements of the ascent curve of the apparatus. This work was supported by NASA Grant No. NAG-110, the Istituto Nazionale di Fisica Nucleare, Italy, and the Agenzia Spaziale Italiana, as part of the research activities of the WIZARD Collaboration. A very special thanks goes out to our technical support staff from NMSU and INFN.

[1] G. D. Badhwar, S. A. Stephens, and R. L. Golden, Phys. Rev. D **15**, 820 (1977).
[2] T. K. Gaisser, Philos. Trans. R. Soc. London A **346**, 75 (1994).
[3] P. Lipari, Astropart. Phys. **1**, 195 (1993).
[4] D. H. Perkins, Astropart. Phys. **2**, 249 (1994).
[5] A. S. Stephens, in *Proceedings of the 17th International Cosmic Ray Conference*, Paris, France, 1981 (CEN, Saclay, 1981), Vol. 4, p. 282.
[6] M. Conversi, Phys. Rev. **79**, 749 (1950).
[7] Ya. L. Blokh, L. I. Dorman, and I. Ya. Libin, Nuovo Cimento Soc. Ital. Fis. **37B**, 198 (1977).
[8] M. Circella *et al.*, in *Proceedings of the 23rd International Cosmic Ray Conference*, Calgary, Canada, 1993, edited by R. B. Hicks *et al.* (World Scientific, Singapore, 1994), Vol. 4, p. 503.
[9] M. P. De Pascale *et al.*, J. Geophys. Res. **98**, 3501 (1993).
[10] R. L. Golden *et al.*, Nucl. Instrum. Methods **A306**, 366 (1991).
[11] J. L. Lacy and R. S. Lindsey, Nucl. Instrum. Methods **119**, 483 (1974).
[12] R. L. Golden *et al.*, PAL technical note No. 224, 1990 (unpublished), available on request.
[13] O. C. Allkofer and P. K. F. Grieder, *Physics Data: Cosmic Rays on Earth* (Fachinformationszentrum, Karlsruhe, Germany, 1984).
[14] R. R. Daniel and S. A. Stephens, Rev. Geophys. Space Phys. **12**, 233 (1974).
[15] A. Codino *et al.*, in *Frontier Objects in Astrophysics and Particle Physics*, Vulcano Workshop, 1994, edited by F. Giovannelli and G. Mannocchi, Conf. Proc. Vol. 47 (Italian Physical Society, Bologna, Italy, 1995), p. 413.
[16] T. K. Gaisser, *Cosmic Rays and Particle Physics* (Cambridge University, Cambridge, England, 1990).